Lasers in Manufacturing Conference 2019

CFD simulations for laser welding of Al alloys

Pareekshith Allu[a*]

[a]*Flow Science Inc., 683 Harkle Road, Santa Fe 87505, USA*

Abstract

To meet stricter fuel economy standards in the automotive industry, automakers have increasingly turned to using aluminum diecast parts and panels due to their light weight and superior castability. Laser welding is a process by which die cast parts are connected to other semi-finished parts, such as profiles or tubes, through pressure-tight joints. However, gasses trapped during casting present challenges to the laser welding process and can cause additional defects such as porosity and melt pool blow-outs. Computational fluid dynamics (CFD) simulations of laser welding help improve the process and achieve superior weldability. In this presentation, case studies on CFD simulations successfully employed to optimize process parameters such as welding speed, laser heat flux profiles, and angles of inclination to mitigate porosity formation are studied. These CFD models serve as an initial, crucial step towards optimization of the process of laser welding of die-cast parts.

Keywords: CFD simulations, laser keyhole welding, FLOW-3D, melt pool dynamics

1. Introduction

CFD simulations help shed light on the laser welding processes at a fundamental level. By accounting for all the relevant physics, melt pool dynamics in a laser welding process can be studied in accurate detail, which help understand the role process parameters play on influencing weld bead dimensions, surface morphology and melt pool related defects such as porosity. The CFD software, ***FLOW-3D***, has implemented relevant physics such as fluid flow, heat transfer, laser melting, phase change, recoil pressure and solidification, which makes it uniquely suited to analyze laser welding processes at the melt pool scale. In this paper, two case studies where researchers from the industry and academia utilize ***FLOW-3D*** to study laser welding processes are presented. In the first case study, a numerical model for full penetration laser welding of carbon steel plates is developed, and the resultant melt pool lengths at the top and bottom surface are compared to experimental data. In the second, remote laser lap welding of Aluminum alloys is carried out,

* Corresponding author. Tel.: +1-505-982-0088;
E-mail address: paree.allu@flow3d.com.

and the computational models developed shed light on the role of process parameters such as welding speed and angle of inclination on the formation of keyhole welding porosity.

2. DESIGN OF EXPERIMENTS

2.1. CASE STUDY 1

A study on full penetration laser welding of a 10mm low carbon steel plate using a 16kW continuous wave think disk laser was carried out by the Korea Advanced Institute of Science and Technology in South Korea in collaboration with State Key Laboratory of Mechanical Behavior for Materials, China and The Federal Institute for Materials Research and Testing, Germany[1]. Two high speed CCD cameras captured the formation of upper and lower surfaces of molten pool during the welding process. It was observed that the lower surface was longer and more unstable than the upper melt surface. To explain this phenomenon, a 3D fluid flow and heat transfer model was developed using the CFD software, ***FLOW-3D***, that incorporates the volume-of-fluid method (VoF) and a ray-tracing algorithm to account for the coupling of the melt pool dynamics with keyhole formation. It is shown that the simulation results are in good agreement with the experimental data while comparing weld cross-sections and melt pool lengths.

2.1.1 Experiment

The laser beam is focused on the workpiece using a 300mm focal length lens.

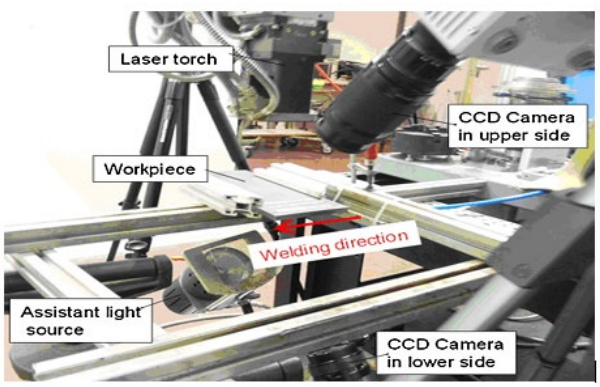

Fig. 1. Photograph of the experimental facilities

Welds with a length of 100mm, were produced with a welding speed of 1m/min and a laser power of 8kW. As seen in Figure 1, two high speed CCD cameras were used to take images of the melt pool surface.

2.1.2 Computational Model

The accuracy of computational models is defined by the extent of the physics models that are implemented to define the process. The following list of models from ***FLOW-3D***[2] is employed

- Molten metal flow is assumed to be Newtonian, laminar and incompressible.
- A Gaussian distribution for the laser beam power is utilized.
- Evaporation induced recoil pressure that controls the amount of heat and mass flux from the melt pool into the void is implemented using the Clausius-Clapeyron equation.

- A ray tracing algorithm tracks the multiple reflections of the laser beam within the keyhole, which affects the total amount of input heat energy into the melt pool according to Fresnel absorption.
- Radiation heat transfer from plasma/vapor to workpiece is accounted for at both top and bottom surfaces.
- Surface tension induced Marangoni convection is also accounted for.

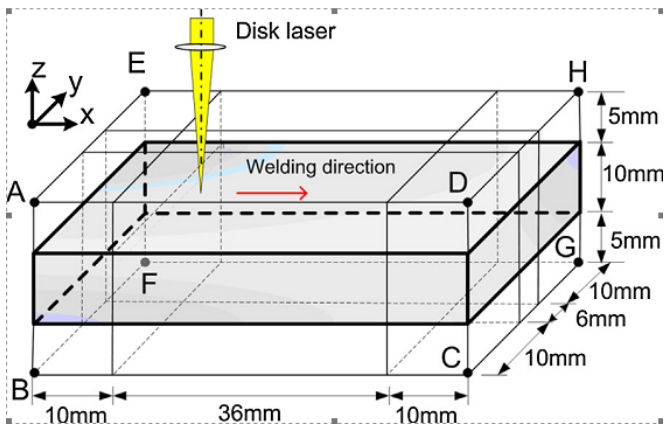

Fig. 2. A schematic of the computational domain

As seen in Figure 2, the computational domain is 56mm in length, 26mm in width, and 20mm in height including the void regions above and below the workpiece to accurately track the free surface. A total of 871,396 uniform mesh cells were utilized. The top boundary and bottom boundary, i.e. ADHE and BCGF in Figure 1 of the computation domain are set as pressure outlet boundaries, while the other four boundaries of computation domain are set as continuative boundaries.

2.1.3 Results and Discussions

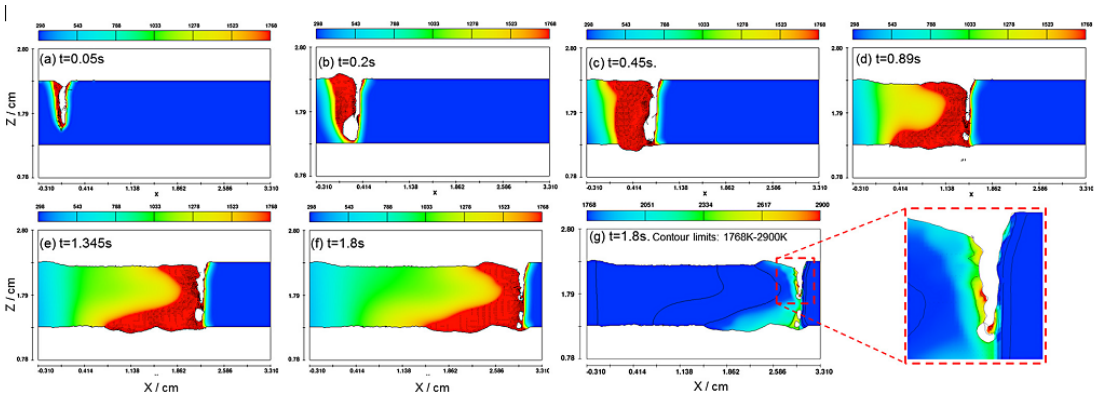

Fig. 3. (a)-(g). Calculated temperature fields and velocity fields in cross-sectional side views

As shown in Figure 3, the temperature and velocity fields are plotted from a cross-sectional side view. After about 200ms, the laser beam fully penetrates the plate thickness and melt pools at the top and bottom surfaces are beginning to form. In Figure 3(g), at about 1.8 seconds, it is seen that temperatures in certain regions of the melt pool reach the evaporation temperature and accordingly experience recoil pressure. It is also seen that the length of the melt pool in the lower surface is much larger than the top surface. In the quasi-steady state, which occurs after about 1.4s and is seen in Figure 4 below, the predicted length of the melt pool is 7.8mm in the top surface, and 15mm in the bottom surface.

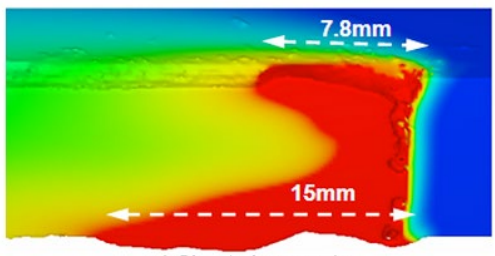

(a) Simulation result

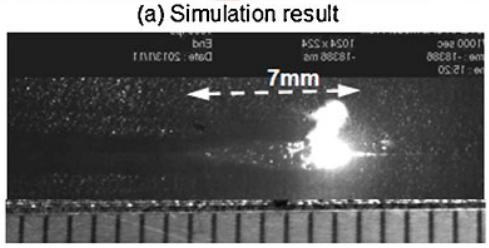

(b) Experiment result: upper surface of molten pool

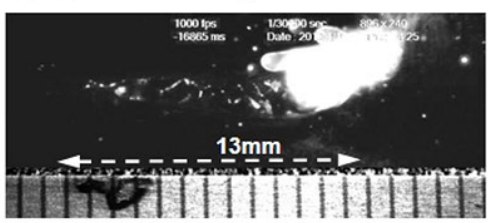

Fig. 4. (a)-(c). Comparison of molten pool lengths between simulation and experiment.

The computed weld pool in figure 4 (a) is shown at t = 1.8s, and is compared to figures 4(b) and 4(c), the experimental CCD images of the top and bottom surfaces of the melt pool are shown. The experimental data indicates that the top molten pool length is around 7mm, whereas the bottom melt pool length is around 12mm, making the simulation results reasonably agreeable.

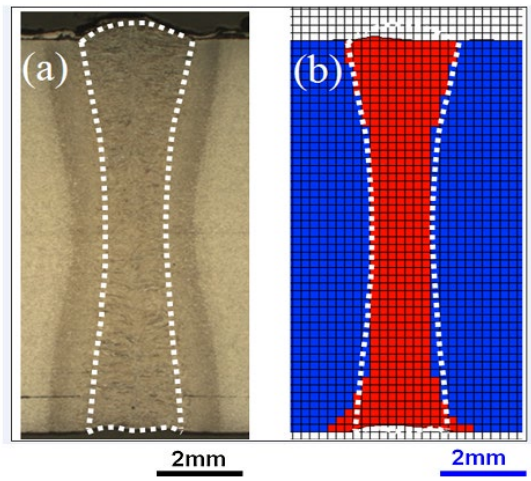

Fig. 5. Comparison of weld cross-section between (a) experiment and (b) simulation.

In figure 5, a comparison of cross-sectional fusion zones between simulation and experiment is shown. The dashed lines are the boundary of experimentally decided fusion zone. Accordingly, the simulated width of the cross-section at the top agrees well with experimental data, while the simulated bottom width of fusion zone is a little longer than the experimental result.

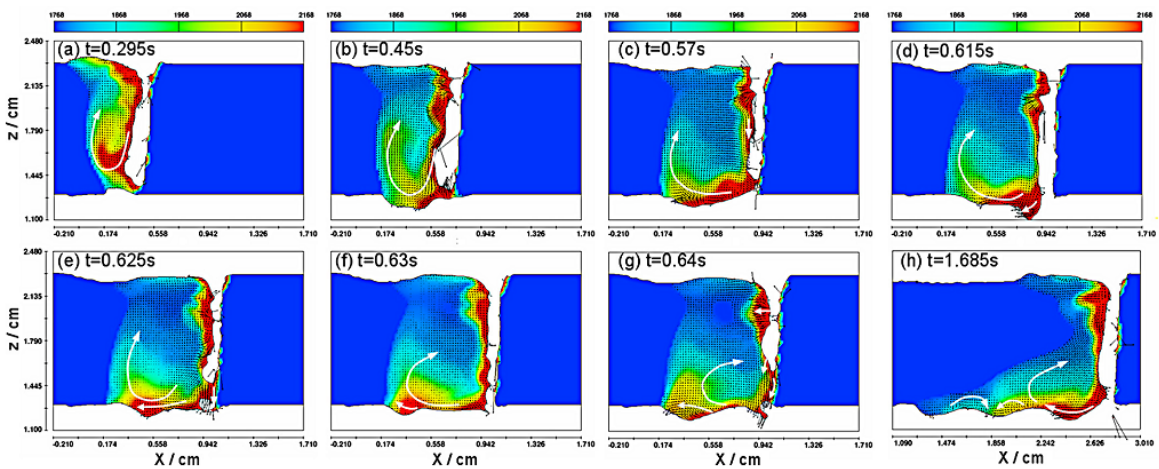

Fig. 6. (a)-(e). Simulation results of the flow pattern of lower part in cross-sectional side views

Figure 6 (a)-(e) shows the transient evolution of the melt pool and it is seen that the size of the lower melt region continues to increase in the initial stage of full laser penetration. This can be explained because of gravity, recoil pressure and a difference in surface tension forces between the top and bottom surfaces. As gravity and recoil pressure push the melt region down, the difference in surface tension forces also contributes to an increasing melt volume at the bottom. The temperatures are also higher near the lower surface and this causes the surface tension forces to be smaller, potentially causing a more unstable molten pool near the bottom.

2.1.4 Conclusions

- A full 3D fluid flow and heat transfer model that incorporates the relevant physics of laser welding is pertinent to explaining the weld dimensions and morphology of full penetration laser welding.
- Because of gravity, recoil pressure and surface tension, the lower melt regions are more unstable and elongated as compared to the top surface.

With the success of the numerical model in explaining full penetration laser welding, the role of welding speed and weld angle of inclination on keyhole laser welding porosity welding porosity is studied in detail next.

2.2. CASE STUDY 2

Keyhole-induced porosity is a major cause of defects in remote laser lap welding of Aluminum joints. Such defects lead to weakened strength joints, and thus it is of importance to understand the mechanism of keyhole and keyhole-induced porosity formation. In this case study, researchers from General Motors, USA and Shanghai Jiao Tong University, PR China developed 3D computational fluid dynamics models using ***FLOW-3D*** to outline the formation of porosity in laser keyhole welding[3]. Void or porosity formation typically takes three steps: a) bubble formation in the melt pool due to collapsing keyholes, b) bubbles floating to the rear molten pool due to convection, and c) bubbles being captured by an advancing solidification front. These processes result in porosity. With better control of process parameters, it is possible to interfere with any of the three steps and so, keyhole-induced porosity can potentially be mitigated. It is observed that high laser welding speeds and large angles of beam inclination, help in creating a quiescent rear molten pool thus stabilizing the keyhole and decreasing the rate of bubble formation.

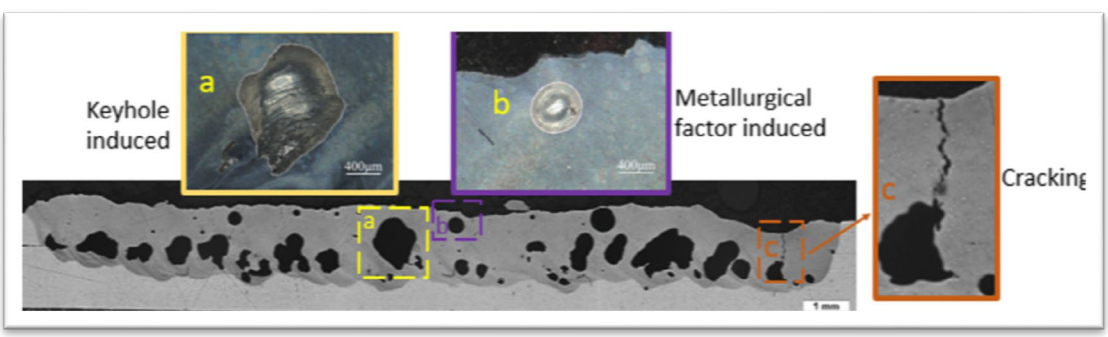

Fig. 7. Pictures of weld porosities in laser-welded Al joint's cross section

As seen in Figure 7, keyhole induced porosity is more irregularly shaped than metallurgically induced porosity due to the influence of process parameters, rather than the influence of trapped gasses. Such porosity can typically lead to cracking.

2.2.1 Experiment

Figure 8 shows the schematic of the remote laser lap welding process of two AA5182 metal plates. The laser beam is an IPG 6kW continuum wave fiber laser system, and two galvo mirrors are utilized to direct the laser beam at specific angles of inclination on to the metal plates.

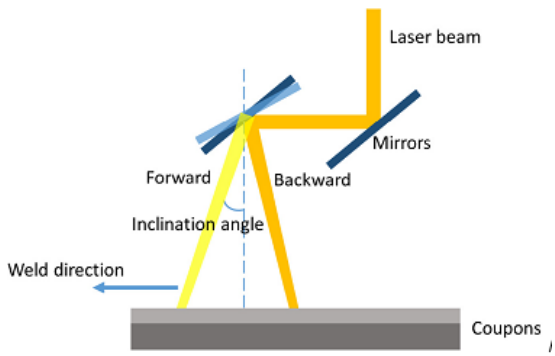

Fig. 8. Schematic of remote laser lap welding process on AA5182 1 mm + 2 mm plates

The 1mm plate is stacked on top of the 2mm plate and the welding is performed with beam's focus plane on the top surface. A beam spot size of 0.6mm is used and a total distance of 25mm is laser welded. The laser scanning speed and beam inclination angle are varied independently and parametrically to evaluate the effects of each parameter on the formation of porosity.

2.2.2 Computational model

The physics implemented in the ***FLOW-3D*** models include laser-material interaction and energy absorption, phase change, recoil pressure, fluid flow, solidification evolution, heat and mass transfer. Multiple laser reflections are calculated based on the incident beam angle and local normal to the metal surface, and simultaneously Fresnel absorption is applied to account for the dependency of heat input into the metal region based on the angle of incidence and other laser and material dependent coefficients.

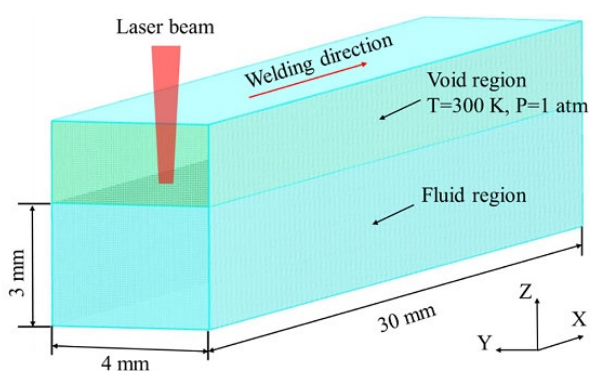

Fig. 9. Illustration of the mesh and computational domain used in the simulation

Figure 9 showcases the mesh used in the computational simulation and indicates the relevant fluid and void regions. The numerical procedure involves the solution of mass, momentum and energy conservation equations using the ***FLOW-3D*** software. Additionally, the free surface is tracked using the VoF method.

2.2.3 Results and discussions

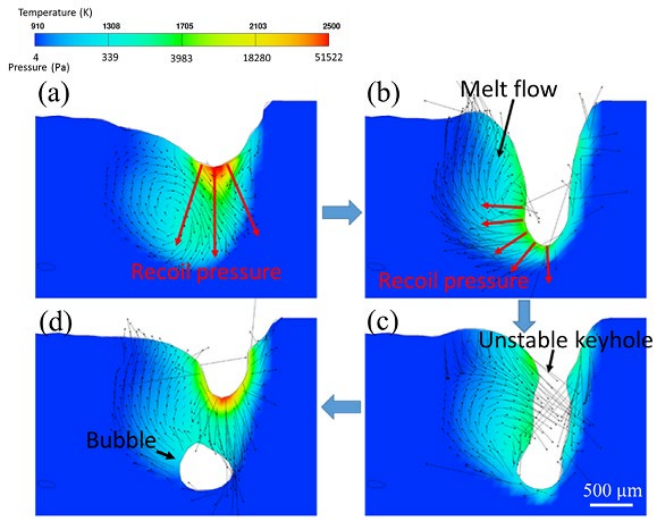

Fig. 10. Process of bubble formation due to keyhole collapsing (P = 2.5 kW, v = 3 m/min): (a) 0.2340 s; (b) 0.2345 s; (c) 0.2350 s; and (d) 0.2355 s.

In Figure 10(a)-(e), the mechanism behind keyhole-induced porosity is shown. As the laser beam shines on the melt pool surface at 0.234 seconds, it causes the melt pool to depress due to evaporation induced recoil pressure. This melt pool depression along with surface tension induced Marangoni convection causes the re-circulation in the rear molten pool, which leads to the rear keyhole wall collapsing on the front keyhole wall, and results in bubbles trapped in the melt pool.

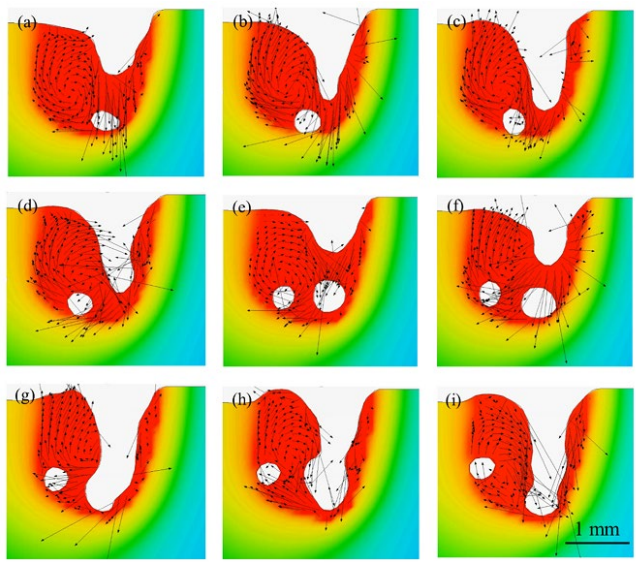

Fig. 11. Process of bubble formation due to keyhole collapsing (P = 2.5 kW, v = 3 m/min): (a) 0.2340 s; (b) 0.2345 s; (c) 0.2350 s; and (d) 0.2355 s.

However, not all bubbles in the melt pool result in porosity. Only when a bubble is captured by the advancing solidification front as seen in Figure 11 (a)-(e) does the trapped bubble become a void. Another bubble that is formed in Figure 11(e) goes on to recombine with the free surface of the melt pool and thus, avoids becoming captured by the advancing solidification front. Next, a parametric study on process parameters is implemented to understand their influence on keyhole induced porosity.

Table 1. Welding process parameters

	Laser Power (kW)	Welding speed (m/min)	Beam inclination angle (^{0})
Effect of welding speed	2.5	3	0
	5	10	0
	6	12	0
Effect of beam inclination angle	2.5	3	-15
	2.5	3	0
	2.5	3	15
	3	3	30
	3	3	45

In Table 1, the laser welding speed is increased from 3m/min to 12m/min while also increasing the laser power to keep the depth of penetration the same. Accordingly, in Figure 12, it is seen that simulations predict a decrease in the formation of porosity, which is also corroborated by the experimental results in Figure 13.

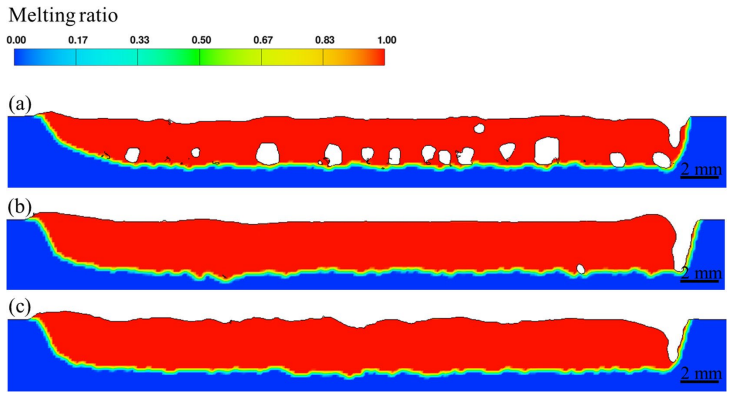

Fig. 12. Distribution of porosity in longitudinal welding sections from simulations with following sets of parameters: (a) P = 2.5 kW, v = 3 m/min; (b) P = 5.0 kW, v = 10 m/min; and (c) P = 6.0 kW, v = 12 m/min.

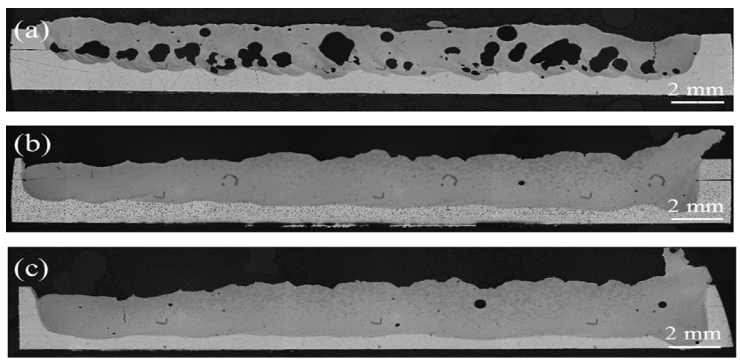

Fig. 13. Distribution of porosity in longitudinal welding sections from experiments with following sets of parameters: (a) P = 2.5 kW, v = 3 m/min; (b) P = 5.0 kW, v = 10 m/min; and (c) P = 6.0 kW, v = 12 m/min.

A look at the process simulations helps discern the reason for high powers and welding speeds being beneficial to the welding joint. It is seen in Figure 14 that at high speeds and powers, the width of the keyhole opening at the top is greater, thus preventing the collapse of the rear keyhole wall onto the front.

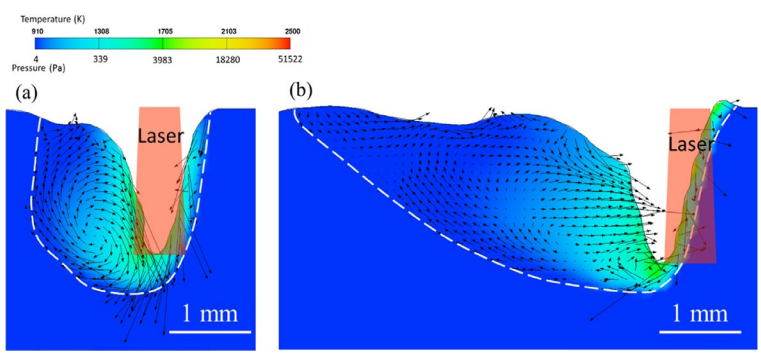

Fig. 14. Predicted velocity fields and temperature distribution in the molten pools, and laser's position relative to keyhole surface for: (a) P = 2.5 kW, v = 3 m/min and (b)P = 6 kW, v = 12 m/min.

Additionally, a large fluctuation in keyhole depth is observed for the low speed and low power case, although the depth of penetration of the laser beam is the same. This change in depth is a likely indication of keyhole collapsing due to the violent nature of melt pool dynamics in the rear keyhole wall. This can be attributed to the laser beam shining on both the front and rear keyhole-walls causing turbulent melt pool dynamics in the rear molten pool. It is also seen in Figure 14 that at large speeds and powers, the melt pool behind the keyhole is elongated, and this is beneficial for the bubbles to escape before getting trapped by advancing solidification fronts. The laser beam also predominantly shines on the front keyhole wall, thus minimizing turbulence in the larger rear molten pool.

Next, the role of laser beam inclination angles on laser welding is studied. Since the optics in remote laser welding are far from the workpiece as compared to conventional laser welding, the inclination angle can influence melt pool dynamics. As listed in Table 1, the angles of inclination are varied between -15^0, 0^0, 15^0, 30^0, and 45^0.

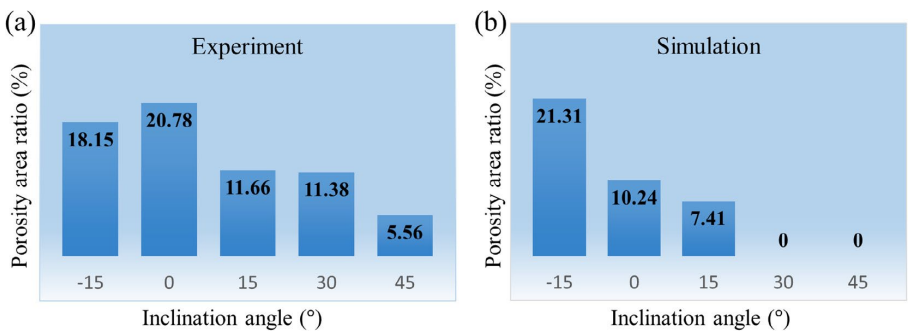

Fig. 14. Pore area percentage at different inclination angle: (a) experiment results and (b) simulation results.

Figure 14 plots the pore area percentages in both experiments and simulations. It is seen that porosity is suppressed with an increase of inclination angle as seen in both experiments and simulations. The experiments show a larger pore area percentage compared to simulations, which can be attributed to the laser beam focal plane being shifted away from the top surface of the weld plates, when the angle of inclination changes. The simulations, on the other hand, make the approximation that the laser beam focal plane is always at the top surface of the weld plates. Nevertheless, the trends predicted are in good agreement.

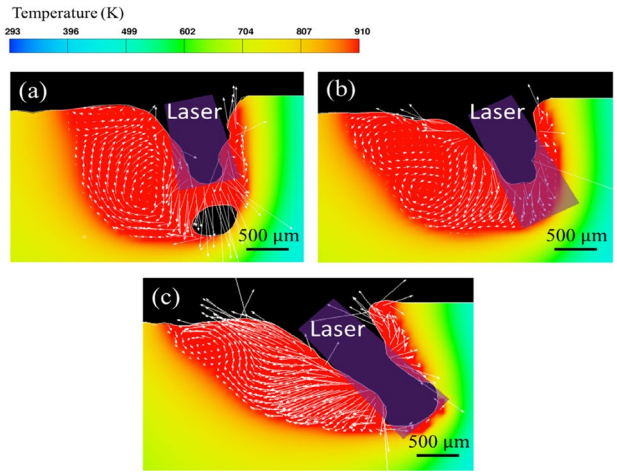

Fig. 15. Calculated velocity fields and temperature distribution in the molten pools for different inclination angles and laser powers: (a) 2.5 kW, 3 m/min and 150; (b) 3 kW, 3 m/min and 300; and (c) 3 kW, 3 m/min and 450.

To understand why larger beam angles of inclination show a reduction in porosity, it is worth investigating the melt pool dynamics as shown in Figure 15. At a 15^0 angle of inclination, there is intense re-circulation observed in the rear molten pool, and the keyhole collapsing with bubble formation is seen. Two vortices are observed at a 300 angle of inclination, which arise due to recoil pressure and surface tension forces, and this causes the rear wall to be less steep compared to the 15^0 angle of inclination rear motel pool wall. Finally, at 450, the rear molten pool now has laminar flow going away from the rear keyhole wall due to gravity and recoil pressure becoming more aligned, thus driving the flow downward and backward. Once again, a more stable rear molten pool eventually leads to mitigation of porosity.

2.2.4 Conclusions

- At high laser power and welding speeds, the keyhole is more stable due to a larger keyhole opening and minimal fluctuation in depth. With the laser beam predominantly shining on the front keyhole, the rear molten pool has quiescent metal flow, and this inhibits the formation of bubble and porosity.
- At large laser beam angles of inclination, laminar flow is once again observed in the rear molten pool instead of vortex flow, due to recoil pressure and gravity acting along the same directions. Once again, pore formation is suppressed.

3. FUTURE WORK

With the establishment of accurate CFD models to understand the role of process parameters in laser welding, the ***FLOW-3D*** models can be further extended to study laser welding of complex die-casting parts, and multi-materials welding. Ultimately, CFD simulations will help welding engineers develop process maps for laser welding of several alloys and die casting parts without the need to carry out expensive experimental trials.

References

1. L.J. Zhang, J.X. Zhang, A. Gumenyuk, M. Rethmeier, S.J. Na, Numerical simulation of full penetration laser welding of thick steel plate with high power high brightness laser, Journal of Materials Processing Technology, Volume 214, Issue 8, 2014.
2. Flow Science, Inc., 2017. FLOW 3D User Manual V11.2.
3. Runqi Lin, Hui-ping Wang, Fenggui Lu, Joshua Solomon, Blair E. Carlson, Numerical study of keyhole dynamics and keyhole-induced porosity formation in remote laser welding of Al alloys, International Journal of Heat and Mass Transfer, Volume 108, Part A, 2017.